Journal of Nuclear Materials 488 (2017) 22–32

Contents lists available at ScienceDirect

Journal of Nuclear Materials

journal homepage: www.elsevier.com/locate/jnucmat

Investigation of Zircaloy-2 oxidation model for SFP accident analysis

Yoshiyuki Nemoto [a, *], Yoshiyuki Kaji [a], Chihiro Ogawa [a], Keietsu Kondo [a], Kazuo Nakashima [b], Toru Kanazawa [b], Masayuki Tojo [b]

[a] Japan Atomic Energy Agency, 2-4 Shirakata, Ohaza, Tokai-mura, Naka-gun, Ibaraki, 319-1195, Japan
[b] Global Nuclear Fuel – Japan Co., Ltd., 2-3-1, Uchikawa, Yokosuka-shi, Kanagawa, 239-0836, Japan

HIGHLIGHTS

- An oxidation model of Zircaloy-2 in air environment was developed.
- The oxidation model was validated by the comparison with oxidation tests using long cladding tubes in hypothetical spent fuel pool accident condition.
- The oxidation model successfully reproduced the typical oxidation behavior in air.

ARTICLE INFO

Article history:
Received 14 November 2016
Received in revised form
21 February 2017
Accepted 2 March 2017
Available online 6 March 2017

Keywords:
Spent fuel pool
Severe accident
Zircaloy-2
Cladding
Air flow rate
Oxidation model

ABSTRACT

The authors previously conducted thermogravimetric analyses on Zircaloy-2 in air. By using the thermogravimetric data, an oxidation model was constructed in this study so that it can be applied for the modeling of cladding degradation in spent fuel pool (SFP) severe accident condition. For its validation, oxidation tests of long cladding tube were conducted, and computational fluid dynamics analyses using the constructed oxidation model were proceeded to simulate the experiments. In the oxidation tests, high temperature thermal gradient along the cladding axis was applied and air flow rates in testing chamber were controlled to simulate hypothetical SFP accidents. The analytical outputs successfully reproduced the growth of oxide film and porous oxide layer on the claddings in oxidation tests, and validity of the oxidation model was proved. Influence of air flow rate for the oxidation behavior was thought negligible in the conditions investigated in this study.

1. Introduction

After the severe accidents in Fukushima Daiichi nuclear power plants (NPP) in 2011, concern for loss-of-cooling or lost-of-coolant severe accident in spent fuel pool (SFP) has been spotlighted [1,2]. The potentiality of a SFP severe accident drawn by aircraft attack on NPP had been noticed after the terrorism in US on September 11, 2001, and research programs on the SFP accident with experiments using mock-up fuel bundles of boiling water reactor (BWR) and pressurized water reactor (PWR) were proceeded under international collaboration. The heating experiments in air environment using mock-up bundles showed that the fuel claddings were drastically oxidized, and in this case the fuel bundles were collapsed [3–5]. Other international programs have been organized in Europe as well. Mock-up fuel bundle tests were conducted in assumption of air inlet for reactor pressure vessel which would occur in occasion of piping rupture in NPP during a severe accident. They reported that the cladding oxidation behavior was much more intense in steam/air mixture or in dry air compared to the oxidation in steam [6–8].

Isothermal oxidation tests such as thermogravimetric (TG) analyses using short samples of cladding have provided the knowledge that oxidation rate increases in air compared to steam or in pure oxygen (O_2) [9–14]. Cross sectional observation of the specimens after oxidation test in air revealed that zirconium nitride (ZrN) was precipitated in porous oxide layers which were grown beneath fractures of dense oxide film on the sample surface [10–15]. From this result, catalytic action of nitrogen (N_2) in air for the oxidation of zirconium (Zr) alloy was suggested, and it was thought that it occurred in connection with O_2 starvation in the narrow space beneath oxide film fracture at the meatal-oxide interface [10].

* Corresponding author.
E-mail address: nemoto.yoshiyuki@jaea.go.jp (Y. Nemoto).

http://dx.doi.org/10.1016/j.jnucmat.2017.03.004
0022-3115/

There have been a limited number of reports on cladding oxidation in air from Japan [16–18]. These previous studies were not conducted for the purpose of SFP accident research, and the published experimental data are thought to be not applicable for the SFP accident evaluation. Detailed investigation on hypothetical SFP accidents is required for the development of safety measures, therefore improvement of severe accident codes by embedding a cladding oxidation model in SFP accident conditions is thought to be important.

The Argonne National Laboratory (ANL) in US and the Institut de Radioprotection et de Sûreté Nucléaire (IRSN) in France have proposed oxidation models for cladding in air environment [9,19]. In addition, simulations using severe accident codes which were modified by introducing these oxidation models have been conducted to calculate the oxidation behavior of mock-up fuel bundles in heating tests in air environment [3,8,20,21]. These oxidation models were constructed for claddings made of alloys such as Zircaloy-4 (Zry4), ZIRLO™, and M5®, while there were only few reports on the oxidation behavior of Zircaloy-2 (Zry2) in air, even though this alloy is widely utilized in BWRs [22,23].

The authors have previously conducted isothermal oxidation tests in air on short samples of Zry2 cladding by using TG analysis apparatus, and reported in detail the oxidation behavior [24–26]. In this work, a model for Zry2 oxidation in air environment was constructed by using these basic data. The constructed oxidation model was applied for simulation of oxidation tests using long cladding tubes of Zry2 in hypothetical SFP accident conditions. The agreement between the calculations and the results of experiments was evaluated to validate the oxidation model. In addition, the influence of air flow rate on oxidation behavior was investigated.

2. Experimental

2.1. Specimen

Zry2 cladding typically utilized in BWRs was applied for oxidation tests in this work [27]. Table 1 shows the chemical compositions of the material. The Zry2 cladding is a tube of 11.2 mm in outer diameter and 0.7 mm in thickness. The cladding was cut into 500 mm in length, and a plug was welded to close the one end of a portion of the cladding. The plug was 5 mm in length and 11.2 mm in diameter. The Zr liner on inner surface of the Zry2 cladding was removed before TG analyses in previous works [24–26], but on the contrary, it was not removed in this work because the cladding sample was closed by the plug and thus the inner surface was not oxidized in the oxidation tests.

2.2. Oxidation tests

Oxidation tests on long cladding samples by applying high temperature thermal gradient along the axial direction were conducted by using the system illustrated in Fig. 1. Dry air was heated by using a gas heater up to 340 °C before it was introduced into the quartz chamber at a constant flow rate of 1840 mℓ/min and 310 mℓ/min, respectively. Air was exhausted from the upper end of the quartz chamber. The upper part of the cladding sample was heated by using an infrared gold image furnace, and the lower part was heated by using two heating mantles to give an aimed temperature distribution. Temperature was measured by using five thermocouples which were spot-welded on the surface of the sample at 10, 90, 170, 270, 450 mm from the upper end of cladding sample. The power control of the infrared gold image furnace is based on temperature data measured by using the thermocouple welded at 90 mm from the upper end of cladding sample. The power of the heating mantles was constantly set maximum through the experiment to keep the temperature of the lower part of cladding at ca. 400 °C. A typical temperature profile during an oxidation test is given in Fig. 2. The temperature profile was controlled in the same way in the oxidation tests at high and low air flow rate condition. In the pre-heating regime, the whole sample was heated up to about 400 °C. After this regime, the power of the infrared gold image furnace was increased to give a high temperature gradient, in which the highest temperature was set to 900 °C or 1000 °C at the position of 90 mm from the upper end, and the lowest temperature was set to 400 °C at the position of 450 mm from the upper end of the sample. The temperature gradient was kept the same for 3600 s, then all heaters were turned off and spontaneously cooled down to the room temperature. The air flow rate was kept constant throughout one oxidation test procedure.

The authors previously conducted steady state analyses on hypothetical SFP accident, in which all cooling water was assumed

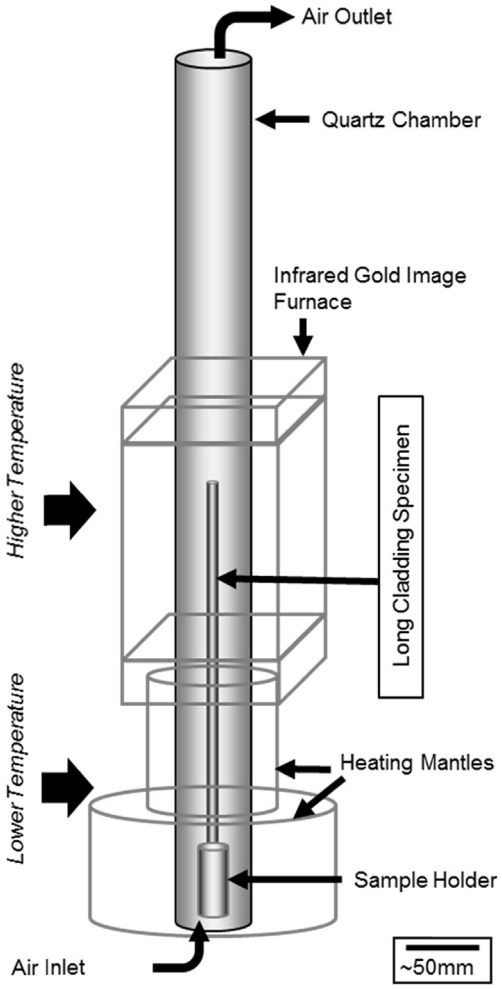

Fig. 1. High temperature oxidation test apparatus designed for long cladding specimens.

Table 1
Chemical compositions of the Zircaloy 2 (wt.%).

Sn	Fe	Cr	Ni	Zr
1.20–1.70	0.07–0.20	0.05–0.15	0.03–0.08	bal.

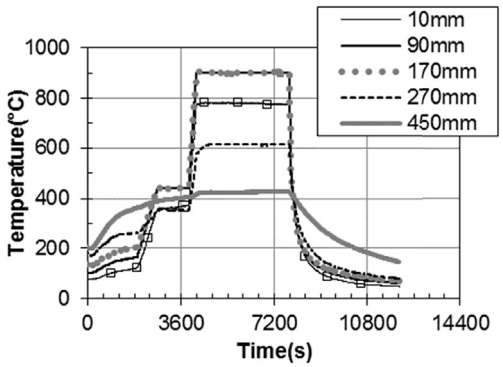

Fig. 2. Temperature profiles during an oxidation test on long cladding sample which was conducted in high air flow rate. Temperatures were measured on positions at five different distances from the upper end of the specimen.

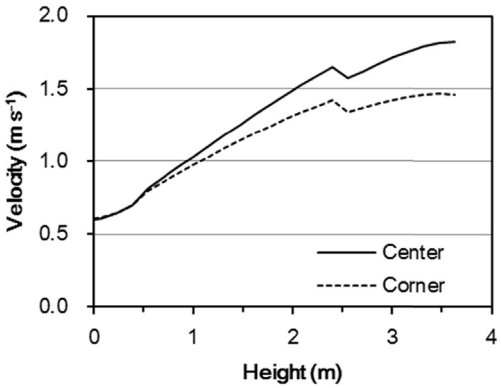

Fig. 3. Velocity of the air flow along axis of the fuel rack at the center of the fuel rack and at the corner of the fuel rack, which were obtained in previous steady state analyses on hypothetical SFP accident with complete loss of the coolant water [28].

to be lost. A 7x10 B-SUS rack containing uranium fuels which were cooled-off for 2 months after the utilization in BWR was modeled in the calculation [28]. The analytical results were referred when testing conditions were determined in this work; however the temperature gradient was set steeper in the tests so that its influence on the oxidation behavior would appear apparent for the evaluation. The air flow rates in the oxidation tests were defined based on the simulation results of the air flow rate in the spent fuel rack. Fig. 3 gives the calculated velocity distribution of the air flow along the axis of the fuel rack at the center of the fuel rack and at the corner of the fuel rack [28]. The quantity of O_2 which was available per second and area of cladding surface was calculated from the analytical results on air flow velocity and information of cross-sectional area of the flow path among claddings in the modeled spent fuel rack. Following this calculation, air flow rates in the oxidation tests were controlled to give the aimed quantity of O_2 on sample surface. The air flow rates in the oxidation tests are summarized in Table 2. The high flow rate in the experiment (1840 mℓ/min: 0.0162 mol/m^2/s of available O_2 on the sample surface) was set to about 20% higher than the highest flow rate (1.8 m/s: 0.0137 mol/m^2/s of available O_2 on the cladding surface) analyzed in the spent fuel rack modeling. The low flow rate in the experiment (310 mℓ/min: 0.0027 mol/m^2/s of available O_2) was set to about 70% lower than the minimum value (0.6 m/s: 0.0046 mol/m^2/s of available O_2 on the cladding surface) in the spent fuel rack so that influence of O_2 starvation in rack for cladding oxidation behavior can be investigated. The O_2 quantities given by the air flow rates in the oxidation tests in this work correspond to the O_2 quantities given by the high and low flow rates (144 and 24 mℓ/min) applied in TG analyses on Zry2 small samples (20 mm in length) which were previously conducted by the authors [24–26].

2.3. Post-test investigations

Detailed observation of the specimen surface after the oxidation tests was conducted by using a field emission scanning electron microscope (FE-SEM) “Sigma”, produced by “Carl Zeiss AG”. After the surface observation, specimens were embedded in resin, and cut along the circumferential direction of the cladding. The cross section was polished by using emery paper in different grit sizes and finally finished with an emery paper with a grit size of ca. 3.0 ± 0.5 μm, which corresponds to number 4000 in Japan industrial standards (JIS) [29], then observed by using optical microscope and FE-SEM. The composition of the oxide layer was analyzed by using a laser Raman spectrometer “NRS-3100” produced by

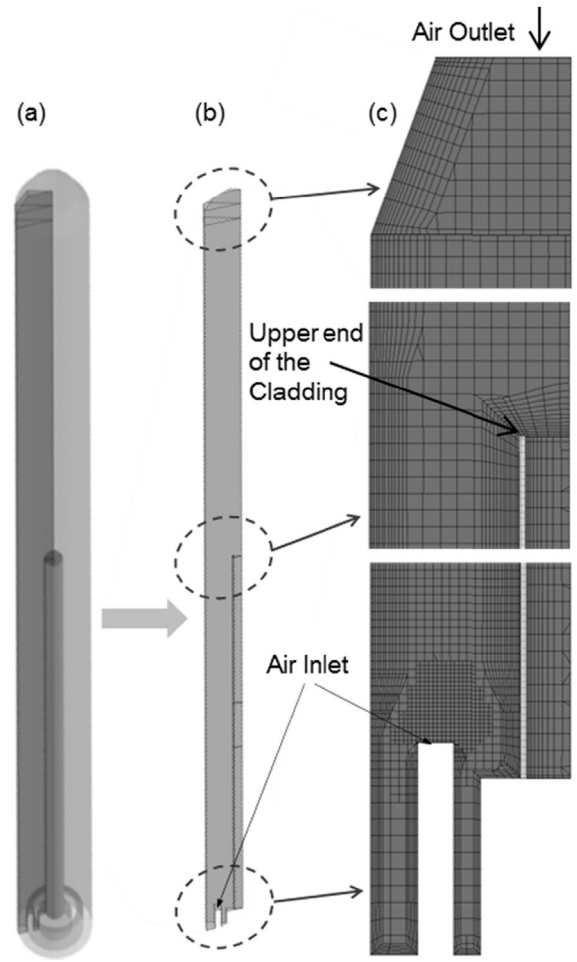

Fig. 4. Analytical model for CFD analyses. (a) whole image of the analytical model, (b) 2 dimensional 1/24 sector model, (c) details of meshing.

“JASCO”, and an Energy Dispersive Spectroscopy (EDS) analysis system “X-Max^N” produced by “Oxford Instruments” which was installed in the FE-SEM. For the laser Raman analyses, the authors referred literature data on Raman spectra obtained in analyses on standard samples or on oxide layers on Zr alloys which were oxidized in air [25,30,31].

Table 2
Air flow rates in the oxidation tests.

Flow rate ID	Air flow rate in oxidation test (mℓ/min)	O_2 flow rate per sample surface (mol/m^2/s)
High	1840	0.0162
Low	310	0.0027

3. CFD analysis

3.1. Modeling of the oxidation test

Computational fluid dynamics (CFD) analyses on the oxidation tests on long cladding samples were conducted by using a commercial code; STAR-CCM+® (ver.10.04)[1]. For the analyses, the unsteady implicit method was adopted [32].

Fig. 4 shows the analytical model for the CFD analysis. A two dimensional 1/24 sector model was used to simulate the test apparatus with the assumption that it is axisymmetric. The total number of the analytical cells was ca. 60000. The air inlet in the actual apparatus was a pipe of 4 mm inside diameter, which was installed at the bottom of the chamber. In the axisymmetric model, the air inlet was modeled as a concentric ring slit which was fixed at the bottom of the chamber. The distance from the axis of the model to the ring slit was fixed as the same as the distance from the axial center of the actual apparatus to the air inlet pipe. The inlet air flow rate in the simulation was set as the same as the experimental condition. The air outlet of the actual chamber had a complicated structure with flange and pipes, but it was simply modeled for the simulation as it can be seen in Fig. 4. In this case, the air flowed out from a hole on the top of the chamber. Preliminary calculation confirmed that this simplification of air inlet and outlet had no influence on the air flow behavior around the cladding sample. In addition, the upper end of the cladding sample was not modeled as it is closed by the plug. Accordingly, the oxidation model was not applied on the inner surface of the cladding to avoid oxidation. In the preliminary calculation, it was indicated that air did not flow into the cladding tube through the open upper end; therefore the influence of this simplification in modeling on the oxidation behavior calculation was thought to be negligible. The temperature distribution measured along the cladding surface in the preliminary oxidation test with the highest temperature of 900 °C was used as a boundary condition. The other boundary conditions are summarized in Table 3.

3.2. Oxidation model for CFD analysis

In CFD analyses on the oxidation behavior of claddings, the chemical reaction of $Zr + O_2 \rightarrow ZrO_2$ was applied. The chemical energy of the oxidation reaction (e.g. −1100.6 kJ/mol at 298.15 K) was taken into account in the calculation. Lasserre et al. proposed a detailed modeling of Zry4 accelerated degradation kinetics, however in consideration of the necessary calculation time for the severe accident code, simple modeling was thought preferable [33,34]. The authors adopted basic equations for oxidation model which were previously proposed by Coindreau et al. for Zircaloy-4 (Zry4) in the temperature range between 600 and 1000 °C [19]. Necessary coefficients for the equation were calculated from the isothermal TG data which were previously obtained on Zry2 in high air flow rate oxidation tests by the authors [24–26]. In this case the applicability of the equation for Zry2 was confirmed by detailed investigation of the TG data. An influence of the air flow rate on the oxidation behavior was not observed below 1000 °C in the range of the flow rate (144 and 24 mℓ/min) applied in the TG analyses by the authors [26]. These air flow rates gave 0.0162 and 0.0027 mol/m^2/s of O_2 on the sample surface. Maeng et al. previously studied the influence of air flow rate on oxidation behavior of Zry4 samples 10 mm in length and revealed that air flow rate below 6 ℓ/h, which gives 0.026 mol/m^2/s of O_2 on the specimen surface, does not change the mass gain behavior during the oxidation tests at 850 °C [35]. The authors previously conducted the TG analyses on Zry2 sample 20 mm in length at air flow rate 250 mℓ/min, and reported that oxidation kinetics were not different from that at air flow rate 144 mℓ/min when oxidation tests were conducted below 1000 °C [26]. Therefore the oxidation model construction in this work was exclusively conducted by using the TG data obtained at high air flow rate (144 mℓ/min).

It is known that during the initial Zr alloy oxidation in air, a dense oxide film grows on the alloy and the oxidation rate decreases [9–11,19]. This phase is called pre-breakaway or pre-transition phase. In this work, parabolic rate kinetics which can be calculated by using the following equation proposed in the literature was applied for this phase [9–11,19];

$$\frac{d(\Delta m/S)^2}{dt} = k_p \tag{1}$$

where, Δm is the mass gain (g), S is the surface area (m^2) of specimen, t is the oxidation time (s), and k_p is the parabolic rate constant (g^2/m^4/s), respectively.

After breakaway, cracks in the oxide film propagate and the oxidation rate accelerates. Natesan et al. applied parabolic rate kinetic, Steinbrück et al. applied linear rate kinetics, and Coindreau et al. applied accelerated rate kinetics for this post-breakaway or post-transition regime, respectively [9,14,19]. In this work, applicability of these kinetics were investigated for the TG data on Zry2 oxidation in air which were previously obtained by the authors [26]. Fig. 5 shows the examples of the plot of TG mass gain data converted by using the equations of the different kinetics in post-breakaway phase of Zry2 oxidation at air flow rate 144 mℓ/min, at 900 °C. In this post-breakaway or post-transition phase, accelerated rate constant which can be calculated by using the following equation was thought most adequate to be applied;

$$\frac{d(\Delta m/S)^{0.5}}{dt} = k_a \tag{2}$$

where k_a is the accelerated rate constant (g$^{0.5}$/m/s).

Temperature dependence of the rate constants are described by using the following equations;

$$k_p = A_1 \exp\left(-\frac{B_1}{RT}\right) \tag{3}$$

$$k_a = A_2 \exp\left(-\frac{B_2}{RT}\right) \tag{4}$$

where R is the perfect gas constant 8.31 J/mol/K and T is temperature (K). A_1, B_1 and A_2, B_2 are coefficients obtained by investigation

[1] STAR-CCM+® is trademark of CD-adapco in the USA or other countries.

Table 3
Boundary conditions of the CFD analyses.

Boundary		Physical condition	Heat transfer condition
Quartz tube:	Inner surface	Solid wall	Isolated (zero emissivity)
Cladding:	Outer surface	Solid wall	Fixed temperature profile
	Inner surface	Solid wall	
	Upper end surface	Solid wall	
Sample folder:	Surface	Solid wall	Isolated
Fluid (air):	Cut-off surface of the 1/24 sector model	Symmetric	Isolated
	Fluid outlet (top of the chamber)	Free outlet (fixed pressure)	Isolated
	Fluid inlet (ring shaped nozzle)	Fixed inlet velocity	Fixed temperature
	Others	Solid wall	Isolated

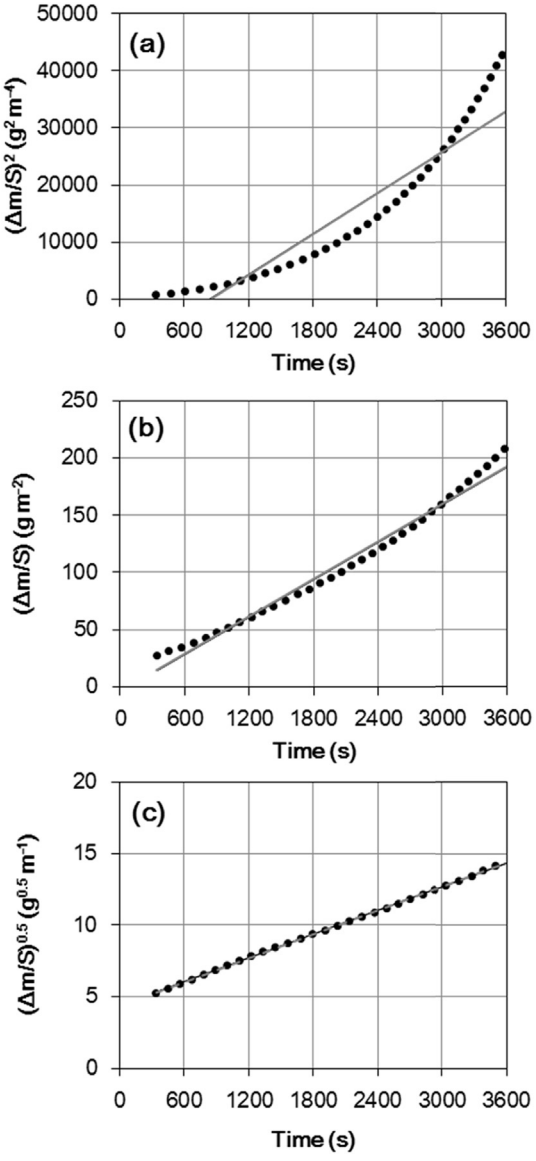

Fig. 5. Mass gain data in post-breakaway phase of Zry2 oxidation at air flow rate of 144 mℓ/min at 900 °C converted by using the equation of (a) parabolic rate kinetic, (b) linear rate kinetics, (c) accelerated rate kinetics are plotted on time.

of the TG data of the oxidation tests. The authors determined these constants based on the results of TG analyses of isothermal oxidation of Zry2 in high air flow rate which were previously reported [24–26].

In this oxidation model, the temperature dependence of mass gain at the breakaway transition is calculated by the following equation;

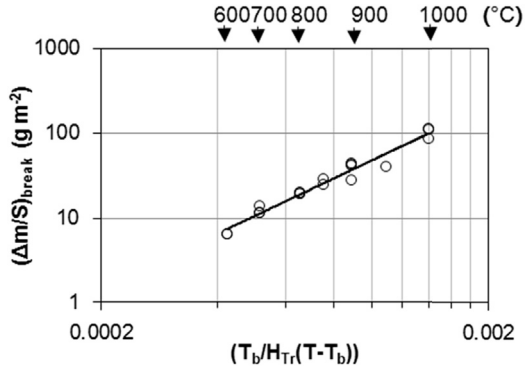

Fig. 6. Mass gain at breakaway transition plotted as function of temperature [24–26].

$$\left(\frac{\Delta m}{S}\right)_{break} = C\left(\frac{T_b}{H_{Tr}(T - T_b)}\right)^D \tag{5}$$

where T_b is the maximum value of the temperature range in which monoclinic zirconia (noted m-ZrO_2) is thermodynamically stable; 1447 K. H_{tr} is the enthalpy of transformation of tetragonal zirconia (t-ZrO_2) to m-ZrO_2; -5.94×10^3 J/mol, and C, D are coefficients which can be obtained by investigation of the TG data on oxidation tests. Here C corresponds to $A^{1/B}$, and D corresponds to $1/B$ in the previous paper by Coindreau et al. [19]. The unit of A is J/mol, and B is a dimensionless number. Detail of this equation is described in the literature [19]. The mass gains at the breakaway transition in the oxidation tests on Zry2 are plotted against the function of temperature in Fig. 6. The values of C, D were obtained by linear fitting of the data points of this graph.

In the oxidation model of Coindreau et al., the oxidation rate after breakaway transition was presumed to continue increasing until total oxidation of the sample at 800 °C and at higher temperatures. Below 800 °C, the oxidation rate after breakaway transition was assumed to increase up to a certain value and then become constant. In this case, the oxidation rate in this final part can be described as linear rate constant (k_l), and it is presumed that oxidation would continue in this rate until total oxidation of the sample [19,22]. The authors had confirmed this tendency in the previous TG analyses on Zry2 oxidation in air [24–26]. Fig. 7 shows the dependence of the linear rate constants (k_l) of Zry2 oxidation on the inverse temperature. In this graph, the values of Zry2 which were given in the literature of Boase et al. are plotted together with the previous data by the authors [19,22,24–26]. The tendencies of the literature data and our own data did not show any problematic difference, therefore the authors adopted the following correlation proposed by Boase et al. for the temperature range below 800 °C;

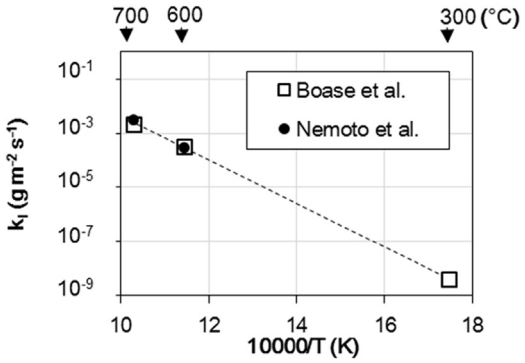

Fig. 7. Linear rate constant as a function of the inverse temperature in previous works [22, 24–26].

$$k_1 = A_3 \exp\left(-\frac{B_3}{RT}\right) \quad (6)$$

where A_3, B_3 are coefficients obtained by the investigation of experimental data [22].

Table 4 summarizes the coefficients determined for equation (3)–(6), based on experimental data. Consequently, these values came out close to the values which were proposed by Coindreau et al. for the Zry4 oxidation. Furthermore the values for the temperature dependence of mass gain at the breakaway transition (C, D) were similar [19]. In the CFD analyses which were proceeded to simulate the growth of oxide layer in the oxidation tests on Zry2 in air environment, these equations and coefficients in the table were applied.

4. Results

4.1. Observation of the oxidized claddings

As it was shown in Fig. 2, the whole cladding sample had been preliminary heated up to ca. 400 °C in air atmosphere in the first stage (~4000 s) of the oxidation tests before it was heated up to the aimed testing temperature. This procedure was adopted because the heating rate of the heating mantle was relatively slower than of the infrared gold image furnace. Due to this reason, it was necessary to turn on the heating mantles earlier so that lower part of the sample could be sufficiently heated. To evaluate the influence of this spare heating stage on the growth of oxide layer, pilot samples were applied for preliminary heating tests. In the preliminary heating tests, only the first stage of the heating procedure was conducted for ca. 4000 s. After these tests, the pilot samples were cooled down to room temperature and used for examinations. These experiments were conducted in high air flow rate as well as in low air flow rate, and it was revealed that surface of the cladding samples turned black in the both air flow rate conditions after the tests. In cross sectional observation of these samples, the oxide layer was not distinguished in optical microscopy, therefore the thickness of the oxide layer was thought to be thinner than 1 μm.

Table 4
List of coefficients for air oxidation model of Zircaloy 2 applied in the CFD analyses.

Pre-breakaway (k_p)	A_1:	1.03×10^8 g^2/m^4/s
	B_1:	1.76×10^5 J/mol
At breakaway transition ($(\Delta m/S)_{break}$)	C[a]:	3.19×10^8
	D[a]:	2.27
First part of post-breakaway (k_a)	A_2:	1.80×10^2 g$^{0.5}$/m/s
	B_2:	1.10×10^5 J/mol
Second part of post-breakaway (k_l) (<800 °C)	A_3:	5.25×10^5 g/m^2/s
	B_3:	1.55×10^5 J/mol

[a] Detail of the units are described in the text.

After the above mentioned preliminary tests, oxidation tests were conducted by applying the whole temperature profile as it was shown in Fig. 2. In this case high temperature thermal gradients with the maximum temperature of 900 °C or 1000 °C was applied on the sample and kept for 3600 s. Oxidation tests with the maximum temperature of 900 °C were successful one time for each high and low air flow rate condition. An oxidation test with the maximum temperature of 1000 °C was successful for high air flow rate condition, while it was not successful for low air flow rate condition because a thermocouple which was used for furnace power control was detached during the test. After the oxidation tests, surface observation was conducted on the samples. Fig. 8 shows the upper part of the samples which includes the region 0–200 mm from the upper end. Fig. 8 (a) shows the sample tested in high air flow rate, and Fig. 8 (b) shows the sample tested in low air flow rate. Both of these were tested with the maximum temperature of 900 °C. Fig. 8 (c) shows the sample tested in high air flow rate with the maximum temperature of 1000 °C.

Around the positions at which thermocouples were spot-welded, fracture of the oxide film was observed. These fractures were thought to have occurred because there were heat-affected zones around the welded points and phase boundaries between thermocouples and cladding. In addition, beige spots and exposure of the base alloy were observed on the welded plugs on the upper end of the claddings. The plugs have the same chemical compositions as the Zry2 cladding, however rolling and other fabrication conditions are different from that of the cladding. Moreover heat during the welding process may have influenced the metallurgy, and caused different oxidation behavior. These areas near the plugs and thermocouples were considered non-prototypical, and therefore excluded in the oxide layer evaluation.

In the region farther than 200 mm from the upper end of cladding, the test temperature was set relatively lower. In this case the sample surface was totally covered by black oxide film, except at the positions on which thermocouples were welded. Fig. 8 shows the region including the upper end of the cladding samples where the test temperature was higher. In the region ca. 50–200 mm from the upper end, which can be seen in the center of Fig. 8, beige spots were observed. The temperature of this area was kept higher than approximately 800 °C during the oxidation test. Fig. 9 shows a FE-SEM image taken at the position ca. 140 mm from the upper end of the sample which was tested in high air flow rate with the maximum temperature of 900 °C. Fractures in the oxide film were observed where beige spots were seen.

Cross sectional observation using the optical microscope was conducted after the samples were cut vertically to the axis of the cladding. The observation was done at different positions to evaluate the dependence of the oxide layer growth on position and on temperature. Fig. 10 gives a typical example of a cross-sectional image obtained at the position ca. 190 mm from the upper end of the sample oxidized in high air flow rate. This position was kept at about 840 °C during the oxidation test. On the surface of this position, beige spots and cracks in the oxide film were observed. In the cross-sectional observation, it was revealed that a porous oxide layer was formed beneath the fracture of the oxide film. At the positions on which black oxide film was formed and no beige spots were observed, dense oxide film was observed in the cross-sectional observation, and it seemed to have uniform thickness on the same circumferential cross section.

Laser Raman spectroscopy was conducted to analyze the chemical compositions of these oxides. Fig. 11 shows typical spectra which were obtained on the cross section of oxide layer on the

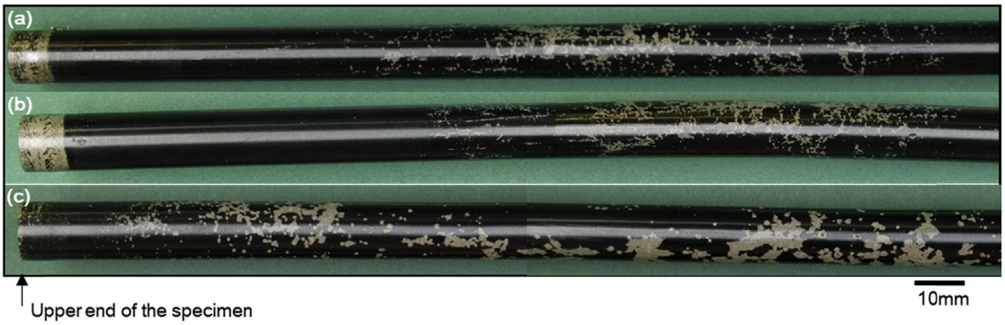

Fig. 8. Post-test appearance of Zry2 claddings after high temperature oxidation test conducted in (a) high air flow rate, (b) low air flow rate.

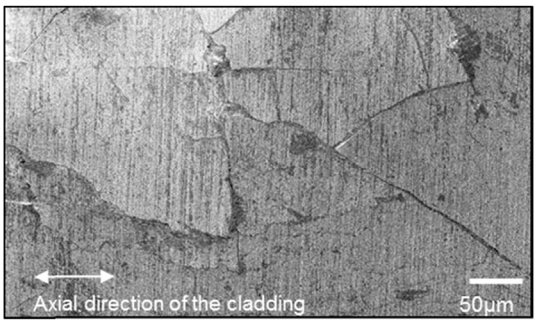

Fig. 9. SEM image of the cladding surface at the position ca.140 mm from the top end, after oxidation test in high air flow rate.

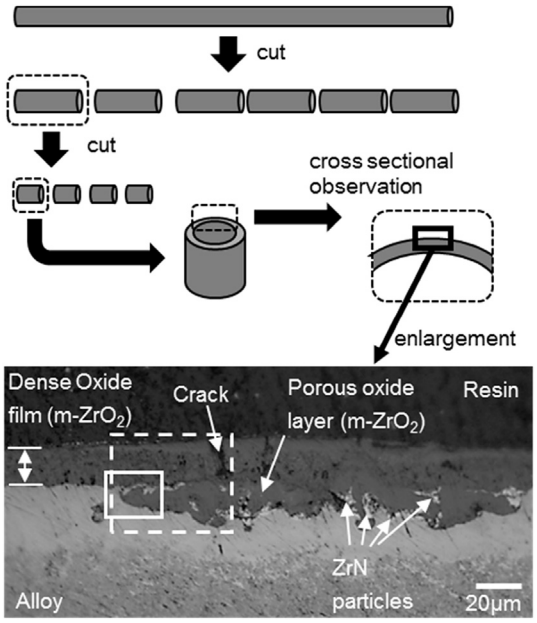

Fig. 10. Typical cross section of the oxide layer formed on the Zry2 cladding after oxidation test in high air flow rate. This position was held at about 840 °C (190 mm from the upper end of the sample) during the test. The area marked by dotted line was analyzed by using laser Raman spectroscopy, and the area marked by solid line was analyzed by using SEM/EDS.

cladding sample after oxidation test in air. After the comparison with the literature data, it was revealed that these were the spectra from the ZrN and m-ZrO_2 [15,30,31]. As it is indicated in Fig. 10 the dense oxide film on the surface is m-ZrO_2, and particles dispersed in the porous oxide layer near the metal-oxide interface were

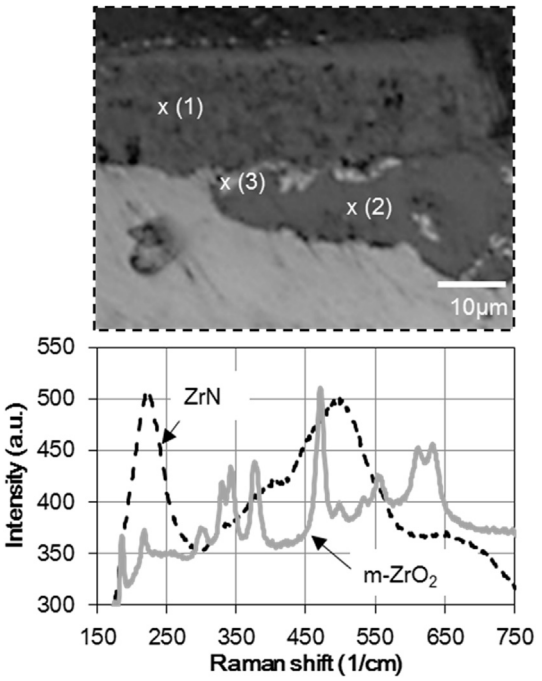

Fig. 11. Typical Raman spectra obtained on cross section of the oxide layer on Zry2 claddings after oxidation tests in air. The spectra of the m-ZrO_2 were obtained at the position (1) and (2), and the spectra of the ZrN were obtained at the position (3), indicated in the picture respectively.

judged to be ZrN. FE-SEM observation and EDS analysis were conducted in the area marked by white solid lines in Fig. 10. Qualitative results are presented in Fig. 12. The oxygen concentration increased in the oxides, and nitrogen concentration was indicated higher in the particles which were judged to be ZrN in the laser Raman spectroscopy.

4.2. Oxide layer growth in experiment and modeling

In the oxidation tests, the power of the infrared gold image furnace was increased after the preliminary heating stage, and thermal gradients such as presented in Fig. 13(a) were applied on the cladding sample and kept for 3600 s. After this high temperature stage, the cladding sample was spontaneously cooled off to room temperature. Plotted temperature values in Fig. 13(a) are the average temperatures in the high temperature holding stage for the duration of 3600 s in the tests with the maximum temperature of 1000 °C in high air flow rate condition, and that with the maximum temperature of 900 °C in high and low air flow rate conditions. In

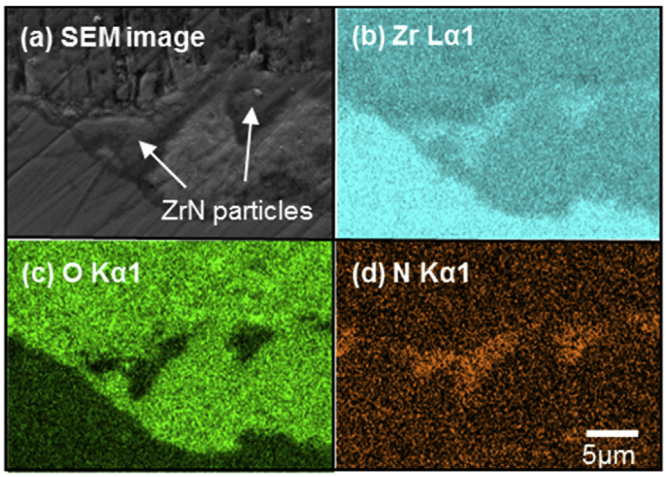

Fig. 12. SEM image on the framed area indicated in Fig. 10, and element maps obtained by using EDS.

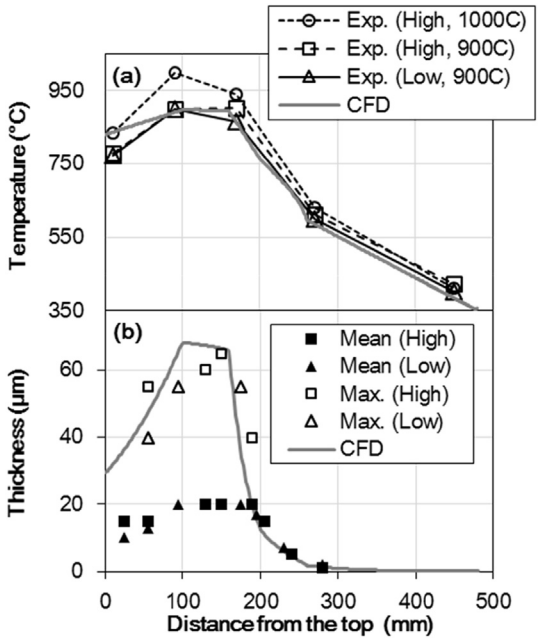

Fig. 13. (a) Temperature distributions along the axis of cladding in experiment and in CFD analysis. Experiments were conducted in high air flow rate with maximum temperature of 1000 °C (○) and 900 °C (□), and in low air flow rate with the maximum temperature of 900 °C (△). (b) Distribution of mean thickness of the dense oxide film on cladding after oxidation tests in high air flow rate (■) and in low air flow rate (▲) with the maximum temperature of 900 °C. The maximum thickness of porous oxide layer on the claddings tested in high air flow rate (□) and in low air flow rate (△) are plotted as well. These were compared to the oxide layer thickness which were calculated in CFD analyses (-) based on the oxidation model.

this graph, the temperature distribution which was given as a boundary condition for the CFD analyses is presented as well. This thermal gradient was determined based on the measured temperatures in the preliminary tests. There was no obvious difference of temperature distribution seen in high and low air flow rates in the preliminary tests, therefore the same thermal gradient was input for the simulations of oxidation tests in different air flow rates.

Fig. 13(b) gives the distribution of the oxide layer thicknesses which were measured after the oxidation tests with the maximum temperature of 900 °C, and which were calculated in the CFD analyses. CFD analyses gave the mass gain in the oxidation calculation, therefore the oxide density value was applied to convert the mass gain to the oxide thickness [36]. The measurements were conducted on the circumferential cross sections of the claddings after oxidation test. Almost uniform thickness was seen for the dense oxide film on the same cross section, therefore in this case mean thickness on each cross section was plotted. Otherwise, the thickness of the porous oxide layer varied even if it is at the same cross section, therefore the maximum thickness on each circumferential cross section was plotted. In the CFD analyses, high and low air flow rates were treated but the same oxidation model was adopted for the different flow rates, therefore calculation of the oxide layer growth provided the same result for the different air flow rate conditions. This is the reason why only one CFD analysis result is shown in Fig. 13(b).

For the region of cladding sample which is closer than 200 mm from the upper end, the temperature was set relatively higher during the oxidation tests. Both dense oxide film and porous oxide layer were observed in this part, and CFD calculation results of the oxide layer thickness was close to the maximum thickness of the porous oxide layer. In the region farther than 200 mm from the upper end of the cladding sample, the oxidation temperature was relatively lower, and only dense oxide films were observed. In this case, the modeling calculated the oxide thickness close to the mean thickness of the dense oxide film. In addition, observations of the dense oxide film and on the porous oxide layer did not show obvious influence of air flow rate on the growth of the oxide layers.

The temperature dependence of the oxide thickness data is summarized in Fig. 14. The temperature values were evaluated by interpolation of the measured data which were obtained on five points on the sample surface by using the thermocouples. Here we have plotted the results of the oxidation tests with the maximum temperature of 900 °C in high and low air flow rate conditions, as well as which with the maximum temperature of 1000 °C in high air flow rate condition. The temperature dependence of the dense oxide film and porous oxide layer thicknesses were not obviously changed by the given maximum temperature or the air flow rate condition. In case the temperature was lower than ca. 800 °C and only dense oxide film was formed, the CFD analyses calculated the oxide thickness close to the mean thickness of the dense oxide film. In case the temperature was higher than ca. 800 °C, dense oxide

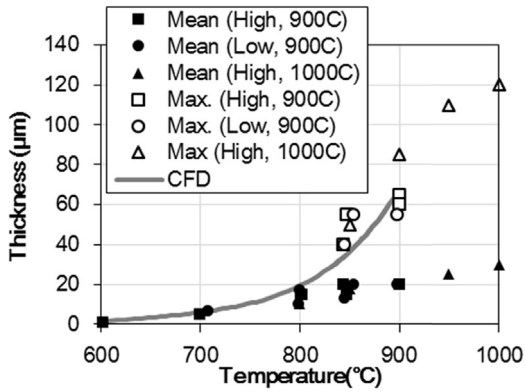

Fig. 14. Temperature dependence of the mean thickness of the dense oxide film observed on cladding surface after oxidation tests with the maximum temperature of 900 °C in high air flow rate (■) and in low air flow rate (●), as well as of the maximum thickness of porous oxide layer on the specimens tested in high air flow rate (□) and in low air flow rate (○). Mean thickness of the dense oxide film (▲) and the maximum thickness of the porous oxide layer (△) on the sample after the oxidation test with the maximum temperature of 1000 °C in high air flow rate are also plotted in the graph. The oxide layer thickness calculated in CFD analyses (-) based on the oxidation model were plotted as well.

film and porous oxide layer were formed on the claddings, and the numerical analyses, which were conducted for the temperature range below 900 °C, provided the results of the oxide thickness close to the maximum thickness of the porous oxide layer which were measured in the experiments.

4.3. Oxygen concentration profile in the modeled test chamber

Fig. 15 shows distributions of O_2 percentage in the atmosphere adjacent to cladding surface along the axis which were calculated in CFD analyses simulating the oxidation tests in this work. In the graphs, the time transitions of the distribution during the high temperature holding stage in oxidation tests are presented. The concentration values presented here were calculated by dividing the content of O_2 by the sum of the contents of O_2 and N_2. O_2 percentage showed the tendency to decrease in the region close to the upper end of the cladding samples in both oxidation tests in high and low air flow rate. To see in detail, the analyzed oxidation rate and the oxygen concentration profile at the position 175 mm from the upper end of the cladding held at 850 °C in high air flow rate are presented in Fig. 16. At the breakaway (~1800 s), jump of the oxidation rate is seen. This was thought because equations of the oxidation kinetics in pre-breakaway and in post-breakaway were separately constructed based on equations (3) and (4) respectively using average TG data. As expected, the oxygen concentration showed the tendency to be in inverse proportion to the oxidation rate. In the CFD analyses in this work, the consumption of O_2 would be the same in different air flow rates because the same oxidation model was adopted in the both cases. But the supply of O_2 is different in different air flow rate condition. This is the reason of the lower O_2 concentration in the off-gas atmosphere in the analysis of the low air flow rate oxidation test.

5. Discussions

5.1. Oxidation mechanism of Zry2 in air

The feature of the oxide layer observed in this work corresponds

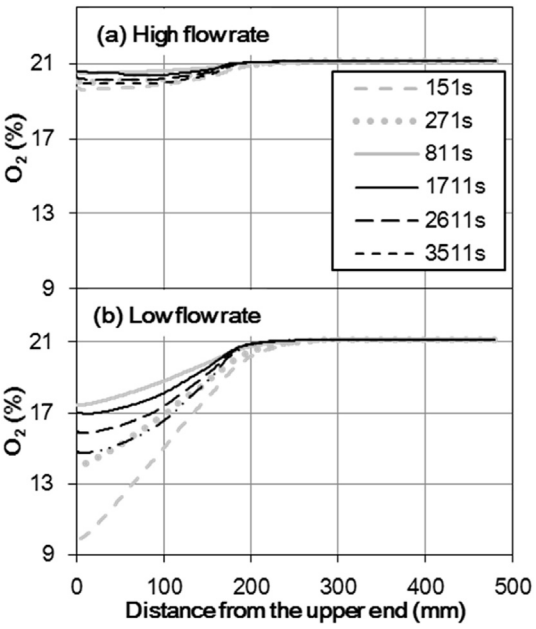

Fig. 15. O_2 concentration along cladding during the oxidation tests in (a) high air flow rate and (b) low air flow rate calculated by CFD analyses.

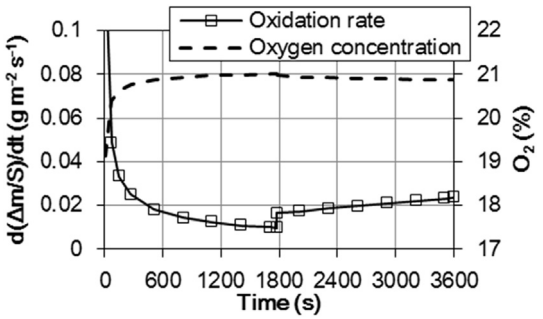

Fig. 16. Calculated oxidation rate and O_2 concentration in the atmosphere adjacent to the surface of the Zry2 long cladding specimen, at the position ca. 175 mm from the upper end, which was held at 850 °C during the simulated oxidation test in high air flow rate.

to the previous knowledge presented in the literature and the works by the authors on Zry4 oxidation in air [9–15,24–26]. Therefore the oxidation mechanism of Zry2 in air seemed close to that of Zry4 despite the little difference of the chemical compositions, etc, as it was previously presented by Steinbrück et al. [23]. The evaluations using the EDS and the laser Raman spectroscopy revealed the formation of ZrN particles in the porous oxide layer beneath the oxide film fracture. If the oxidation mechanism of Zry2 could be considered as same as which of Zry4, it is assumed that the ZrN particles were formed in connection with oxygen starvation in the narrow space below oxide film fracture. In addition, the porous oxide layer is formed in relation with re-oxidation of the ZrN particles. The porous oxide layer seemed to be swelled and pushing up the oxide film. Therefore the formation of the porous oxide layer seems to support propagating of the oxide film to break. In this case, ZrN would be newly formed under the new fracture of oxide film, and help porous oxide layer to grow [37]. Repetition of this process and increasing affected surface can be considered as the mechanism of accelerated oxidation behavior in the post-breakaway transition regime in high temperature oxidation of Zry2 in air.

5.2. Reproducibility of the oxide layer growth

TG data were used in this study to construct the oxidation model, and TG data such as oxidation rates are the macroscopic data which are based on the measurement of the mass gain of the sample. In spite of this, the oxidation model developed in this work successfully reproduced not only the mean thickness of the dense oxide film, but also the maximum thickness of the porous oxide layer which were observed in the experiments. Details of the correspondence between TG data and oxide layer growth are discussed in this section.

The authors previously conducted the TG oxidation tests on Zry4 short samples at 900 °C in high air flow rate which corresponds to the high air flow rate in this work [26]. Several test durations were adopted in the experiments, and in the cross sectional observation after the oxidation tests, cross sectional area of the oxide layers were measured on the photos. These data were used together with the density value of the m-ZrO_2 in a literature [36], to calculate the mass gain derived from the observed growth of oxide layer in different duration of the oxidation tests. Results of the calculation were compared with the mass gain data provided by the TG analyses. The mass gain evaluated on the photos well corresponded with the TG data, and revealed that the TG mass gain data during pre-breakaway regime corresponded to the mass gain derived from the growth of the dense oxide film. In addition, the TG mass gain

data during the post-breakaway regime corresponded to the mass gain derived from the growth of the porous oxide layer. In the post-breakaway regime, growth of dense oxide film was not observed. This correspondence between TG data and the growth of the oxide layers are thought to be the origin of the successful CFD analyses of the oxide layer growth which were conducted by using the oxidation model based on TG data. Randomness and porosity of the porous oxides formed during the post breakaway phase were not taken into account when the calculated mass gain in CFD was converted into oxide thickness. Therefore the calculated thickness was expected to correspond to the average thickness of the oxide layer, however it corresponded to the maximum thickness. To define the reason of this correspondence, further detailed study considering the randomness and porosity of the oxide layer is thought necessary. In addition, it was seen that a thermal gradient along the cladding axis did not bring any problematic discrepancy between the results of experiment and simulation.

The successful reproduction of the oxide layer confirmed the applicability of the oxidation model for the simulation of oxidation behavior of Zry2 long cladding in hypothetical SFP accident condition. Further mock-up tests simulating the SFP accident condition are thought necessary to validate its general applicability, but the proposed Zry2 oxidation model is thought useful as a preliminary model for the severe accident code upgrade for the SFP accident analyses.

5.3. Oxidation behavior and air flow rate

In this work, oxidation tests on Zry2 cladding were conducted in two different air flow rates (called high and low) which were settled to simulate the hypothetical SFP accident condition. Cross sectional observations were conducted after the oxidation tests, and revealed that influence of air flow rate on the oxide layer growth and its morphology was negligible. These results correspond to the TG analysis results in the isothermal condition below 1000 °C [26]. Therefore it can be evaluated that difference of the air flow rate has no influence on the oxidation behavior of Zry2 in the range which was treated in this study.

The authors previously conducted isothermal oxidation tests on Zry2 in the temperature range higher than 1100 °C [26]. In these experiments, the oxidation rate was increased depending on the air flow rate. These experiments were conducted in the same air flow rate range which was applied in this work. Literature suggested that the air flow rate may have a strong influence on the oxidation behavior of the Zry4 [10,35]. If the level of air flow rates were compared in consideration of the available oxygen quantity on the specimen surface per second, the air flow rate conditions in these literature were generally higher than which applied in our work in consideration of the SFP accidents. Duriez et al. conducted the oxidation tests in the range of 0.07–0.36 mol/m^2/s of O_2 available on the sample surface [10], and Maeng et al. conducted the tests in the range of 0.013–0.136 mol/m^2/s [35], whereas the authors tested in the range of 0.0027–0.016 mol/m^2/s. From these knowledges, the authors suggest that further investigation on the air flow rate influence on the oxidation behavior of cladding should be performed in case that higher air flow rate would be expected in future SFP accident investigation.

5.4. Oxidation behavior and atmosphere composition

The result of the CFD analysis given in Fig. 15(b) showed that the O_2 concentration became the lowest at the closest region to the upper end of cladding, especially at the beginning of the oxidation test, e.g. it was ca. 10% in the minimum which can be seen in the graph. However for the most part of time during the oxidation test, oxygen decrease was in the range of ca. 3–5%. In addition, despite the difference of the O_2 concentration in different air flow rates which can be seen in Fig. 15, cross sectional observation did not reveal any obvious influence of this on the oxide layer development. Therefore the decrease of oxygen in the atmosphere in the range which was suggested in this work was thought to have no influence on the oxidation behavior of the cladding.

Oxidation tests in this paper were conducted by using cladding samples 500 mm in length, whereas the actual spent fuel rack is more than 4000 mm in length. Therefore lowering of the oxygen concentration will become more severe in the actual rack than in the oxidation test chamber, especially in the upper part of the rack which would be the downstream of the air flow. Steinbrück et al. studied the influence of O_2 concentration in O_2/N_2 mixed atmosphere on oxidation behavior of Zry4 at 800 °C, 1000 °C and 1200 °C, and found that oxidation became most remarkable in the atmosphere with O_2 concentration of 10–90% [14,23]. They also revealed that oxidation of Zry4 was suppressed in pure N_2 gas or in oxygen starvation condition in O_2/N_2 mixture. From this result it is supposed that decrease of O_2 concentration in the upper part of the spent fuel rack would suppress the oxidation of the cladding.

Oxidation tests in this study were conducted in dry air, meanwhile in a previous report it was presented that sometimes oxidation rate increased in a mixed atmosphere of steam and N_2 compared to dry air according to the effect of hydrogen [38–40]. It can be assumed that in some case, atmosphere in the spent fuel rack during SFP accident would contain both steam and air, therefore the influence of the mixed atmosphere of steam and air is recommended to investigate.

6. Conclusions

In this work, an oxidation model of Zry2 was constructed based on TG data, with the aim of applying it for SFP accident analysis. High temperature oxidation tests on Zry2 cladding sample 500 mm in length were conducted in hypothetical SFP accident conditions in high and low air flow rates. CFD analyses on the oxidation tests were done by using the constructed oxidation model. Results of the oxidation tests and the CFD analyses were compared to validate the oxidation model. Finally, the following outcomes were obtained:

(1) In the oxidation tests applying high temperature with thermal gradient on long cladding samples in air for 3600 s, a black oxide film was formed on the surface. This oxide film was sound on the part in which lower temperature was applied, whereas fractures of the oxide film were seen in the area heated up to the temperature higher than 800 °C. In this case porous oxide layers containing ZrN particles were observed beneath the fractures. The influence of the air flow rate on the oxidation behavior was not clearly seen in the range which was treated in this study to simulate SFP accident.
(2) CFD analyses using the oxidation model which were constructed in this work, were conducted to simulate the oxide layer growth in the oxidation tests on long Zry2 cladding samples. In case of surface oxide film was sound, the simulation reproduced the mean thickness of the oxide film. In the meantime, the simulation reproduced the maximum thickness of the porous oxide layers when these were formed beneath the fracture of the surface oxide film. From these results, the oxidation model was validated, and proved that it is applicable for the Zry2 cladding oxidation in hypothetical SFP accident conditions.
(3) The influence of air flow rate on the oxide layer growth was not clearly seen in the experiments. Oxygen depletion in the

spent fuel rack would occur in the SFP accident, however investigation in this study suggested that it would not have bad influence on oxidation behavior of the cladding.

Funding

This work was conducted as a part of “Severe Accident code upgrading project” in fiscal year 2015 funded by the Ministry of Economy, Trade and Industry of Japan (20151125-3).

References

[1] N. Trégourès, M. Adorni, H. Esmaili, W. Grant, T. Hollands, Z. Hózer, B. Jäckel, M. Muñoz, T. Nakajima, F. Rocchi, M. Stručić, P. Vokac, Nuclear Safety NEA/CSNI/R 2, 2015.
[2] S. Nishimura, R. Hiwatari, M. Furuya, Y. Nishi, CRIEPI Research Report L12007, 2013 (in Japanese).
[3] E.R. Lindgren, S.G. Durbin, NUREG/CR-7143, SAND 2007-2270, 2007.
[4] E.R. Lindgren, S.G. Durbin, NUREG/CR-7144, SAND 2008-3938, 2008.
[5] M. Adorni, L.E. Herranz, Th Hollands, K. Ahn, Ch Bals, F. D'Auria, G.L. Horvath, B.S. Jaeckel, H. Kim, J. Lee, M. Ogino, Z. Techy, A. Velazquez-Lozad, A. Zigh, R. Rehacek, Nucl. Eng. Des. 307 (2016) 418–430.
[6] M. Steinbrück, A. Miassoedov, G. Schanz, L. Sepold, U. Stegmaier, J. Stuckert, Nucl. Eng. Des. 236 (2006) 1709–1719.
[7] J. Stuckert, Z. Hózer, A. Kiselev, M. Steinbrück, Ann. Nucl. Energy 93 (2016) 4–17.
[8] E. Beuzet, F. Haurais, C. Bals, O. Coindreau, L. Fernandez-Moguel, A. Vasiliev, S. Park, Ann. Nucl. Energy 93 (2016) 18–27.
[9] K. Natesan, W.K. Soppet, Argonne National Laboratory Report ANL/03-32, NUREG/CR-6846, 2004.
[10] C. Duriez, T. Dupont, B. Schmet, F. Enoch, J. Nucl. Mater. 380 (2008) 30–45.
[11] C. Duriez, M. Steinbrück, D. Ohai, T. Meleg, J. Birchley, T. Haste, Nucl. Eng. Des. 239 (2009) 244–253.
[12] M. Steinbrück, J. Nucl. Mater. 392 (2009) 531–544.
[13] M. Steinbrück, M. Böttcher, J. Nucl. Mater. 414 (2011) 276–285.
[14] M. Steinbrück, S. Schaffer, Oxid. Met. 85 (2016) 245–262.
[15] I. Idarraga, M. Mermoux, C. Duriez, A. Crisci, J.P. Mardon, J. Nucl. Mater. 421 (2012) 160–171.
[16] T. Nakayama, T. Koizumi, J. Jpn. Inst. Met. 31 (7) (1967) 839–845 (in Japanese).
[17] J. Nakamura, M. Hashimoto, T. Otomo, S. Kawasaki, J. Nucl. Mater. 200 (1993) 256–264.
[18] T. Arima, K. Miyata, K. Idemitsu, Y. Inagaki, Prog. Nucl. Eng. 51 (2009) 307–312.
[19] O. Coindreau, C. Duriez, S. Ederli, J. Nucl. Mater 405 (2010) 207–215.
[20] E. Beuzet, J.-S. Lamy, A. Bretault, E. Simoni, Nucl. Eng. Des. 241 (2011) 1217–1224.
[21] J. Stuckert, Z. Hózer, A. Kiselev, M. Steinbrück, Ann. Nucl. Energy 93 (2016) 4–17.
[22] D.G. Boase, T.T. Vandergraaf, Nucl. Tech. 32 (1977) 60–71.
[23] M. Steinbrück, SFP Project Seminar 2013, OECD Conference Center, Paris, 2013.
[24] Y. Nemoto, C. Ogawa, Y. Kaji, K. Nakashima, M. Tojo, D. Goto, Proc. 21th International QUENCH Workshop, Karlsruhe, Germany, 2015.
[25] Y. Nemoto, Y. Kaji, C. Ogawa, K. Nakashima, T. Kanazawa, M. Tojo, D. Goto, Proc. 2016 Jpn. Conf. Materials and Environments, A-307, JSCE, 2016 (in Japanese).
[26] Y. Nemoto, Y. Kaji, C. Ogawa, K. Nakashima, M. Tojo, Zairyo-to-Kankyo, (2017), in press, in Japanese.
[27] JIS H4751 (1998), in Japanese.
[28] D. Goto, K. Kobayashi, M. Tojo, T. Ikehara, Y. Kaji, Y. Nemoto, 2015 Fall Meeting of the Atomic Energy Scociety of Japan, F03 (2015), in Japanese.
[29] JIS R6001 (1973), in Japanese.
[30] A. Cassinese, M. Iavarone, R. Vaglio, M. Grimsditch, S. Uran, Phys. Rev. B 62 (21) (2000) 915–918.
[31] X.-J. Chen, V.V. Struzhkin, S. Kung, H.-K. Mao, R.J. Hemley, A.N. Christensen, Phys. Rev. B 70 (014501) (2004) 1–6.
[32] CD-adapco Inc, User Guide - STAR-CCM+ Version 10.04, 2015.
[33] M. Lasserre, V. Peres, M. Pijolat, O. Coindreau, C. Duriez, J.-P. Mardon, Mater. Corros. 65 3 (2014) 250–259.
[34] M. Lasserre, V. Peres, M. Pijolat, O. Coindreau, C. Duriez, J.-P. Mardon, J. Nucl. Mater. 462 (2015) 221–229.
[35] Y. Maeng, M. Steinbrück, M. Große, J. Lee, in: Proc. 21th International QUENCH Workshop, 2015. Karlsruhe, Germany.
[36] M. Suzuki, H. Saitou, Y. Udagawa, JAEA-Data/code 2010–035, 2011 (in Japanese).
[37] M. Steinbrück, J. Nucl. Mater. 447 (1–3) (2014) 46–55.
[38] J. Sung, M. Steinbrück, M. Große, J. Lee, in: Proc. 21th International QUENCH Workshop, 2015. Karlsruhe, Germany.
[39] M. Große, M. Steinbrück, Y. Maeng, J. Sung, Proc. ICA PP 2016, vol. 3, 2016, pp. 2103–2111.
[40] M. Steinbrück, M. Große, F.O. da Silva, Proc. ICAPP 2016, vol. 1, 2016, pp. 535–545.